# CrystEngComm

Accepted Manuscript






ROYAL SOCIETY OF CHEMISTRY

www.rsc.org/crystengcomm

# Precise Control of Configuration, Size and Density of Self-assembled Au Nanostructures on 4H-SiC (0001) by Systematic Variation of Deposition Amount, Annealing Temperature and Duration

Ming-Yu Li,[a] Mao Sui,[a] Puran Pandey,[a] Quan-zhen Zhang,[a] Sundar Kunwar,[a] Gregory. J. Salamo,[b] and Jihoon Lee* [a,b]

[a] College of Electronics and Information, Kwangwoon University, Nowon-gu Seoul 139-701, South Korea. E-mail: jihoonleenano@gmail.com.

[b] Institute of Nanoscale Science and Engineering, University of Arkansas, Fayetteville AR 72701, USA.

The precise control over the configuration, size and density of Au nanoparticles (NPs) has offered an efficient route to enhance and optimize the performance and usability of various NP-based applications. In this study we successfully demonstrate the precise control of configuration, size and density of the self-assembled Au nanostructures on 4H-SiC (0001) via the systematic variation of deposition amount, annealing temperature and duration. Depending on the deposition amount at fixed annealing temperature and duration, the self-assembled Au NPs are successfully fabricated based on the Volmer-Weber growth model, and the NPs nucleate as round-dome shape and evolve into the hexagonal nano-crystals with the facet formation along with the increased deposition amounts. For the variation of annealing temperatures, the Au nanostructures radically develope into two distinct regimes: i.e. irregular Au nano-mounds (Regime I) between 400 and 700 °C based on the diffusion limited agglomeration (DLA) model and round-dome shaped droplets (DPs) (Regime II) between 750 and 900 °C. Depending on the dwelling time, the size and density evolution of round-dome shape Au DPs are dicusscussed based on the Ostwald-ripening theory.

## I. Introduction

Au NPs possess an enlarged surface area-to-volume ratio and the existence of Au NPs can result in increased reaction area,[1-3] distinctive contact interfaces[4] and enhanced coupling.[5] In addition, the collective oscillation of exited electrons at the surface of Au NPs leads to an enhanced electromagnetic field, known as the localized surface plasmon resonance,[6,7] which can lead to the increased light conversion efficiency[8,9]. Furthermore, Au NPs can act as a catalyst[10-12] as well as a nanoscale surface drilling medium for the fabrication of various nanostructures[13,14]. As a result, the precise control over the size, density and configuration of Au nanoparticles (NPs) has found as a promising route to improve and/or optimize the performance of various NP-based applications. For example, due to their superior catalytic capacity, Au NPs can be utilized for the fabrication of nanowires (NWs), in which the crystallization of target vapors can occur at the liquid and solid interface based on the vapor-liquid-solid growth mechanism,[10-12] and thus, the length, diameter,[10] configurations,[11] and even growth direction[12] of NWs can be inherently determined by those of Au NPs. For example, the zigzag Si nanowires were fabricated with extended length and diameter by utilizing the Au NPs with lager size.[10] Meanwhile, the kinking resulted from the strain introduced by the Au NPs during the crystallization can efficiently control the facets formation of the NWs,[11] and the changes of the edge tension with various size of Au NPs can directly govern the growth orientation of the NWs.[12] In addition, the surface etching using NPs is often adapted to fabricate the nanoscale holed templates for further nanostructure growths without the necessity of the chemical solutions and strain formation: i.e. nanoholes formation on $SiO_2$, $Si_3N_4$[13] and Si[14]. Meanwhile, due to the large bandgap (~ 3.23 eV), high thermal conductivity, temperature and current tolerance, and transparency over a broad frequency range, SiC has been widely adapted in high-power field effect transistors, light emitting diodes, resonators, and photodetectors.[15-19] Recently, the guided growth of highly coherent, horizontal GaN NWs on SiC (0001) was successfully demonstrated.[20] The

capability of controlling the configuration, size and density of the Au NPs on SiC (0001) can provide a critical reference for the related applications, which, however, is still rarely reported up to date. In our previous report[21], we demonstrated two distinct evolution processes of Au nanostructures occurred with an annealing temperature variation on 4H-SiC (0001). The irregular nano-mounds at relatively lower annealing temperature was followed by the formation of granules and hillocks, which was regarded as agglomeration of Au due to the limited diffusion. Au NPs were formed with sufficient thermal energy and the final shape of Au NPs can be controlled with the control of deposition amount. In contrast to our previous results, in this paper, we propose efficient approaches to control the configuration, size and density of self-assembled Au nanostructures on 4H-SiC (0001) by means of the variation of deposition amount, annealing temperature and dwelling time. With the variation of the deposition amount, self-assembled round-dome shaped Au NPs are successfully fabricated on 4H-SiC (0001) and gradually evolve into the polyhedral nano-crystals with the increased deposition amounts based on the Volmer-Weber growth model. Au NPs very sensitively respond to the deposition amount variation, which results in the drastic size and density alteration along with the configuration transition. With the annealing temperature variation, the nucleation and evolution of self-assembled Au NPs show two distinctive regimes: irregular Au nano-mounds (Regime I) and round-dome shaped Au droplets (Regime II), and the evolution process is discussed based on the diffusion limited aggregation (DLA) model[22,23] in conjunction with the thermodynamic diffusion theory. With the expended dwelling time, the evolution of the size and density of the Au NPs are discussed based on the Ostwald-ripening.[24,25]

## II. Experimental

In this work, as-received N-type 4H-SiC (0001) wafer was utilized as a substrate. The wafer was ~ 250 μm-thick with an off-axis of ± 0.1° from the Technology and Devices International

(TDI, USA). Fig. S1 shows the Raman spectra of the bare SiC wafer excited with a CW diode-pumped solid-state (DPPS) laser of a wavelength of 532±1 nm with an output power of 120 mW and the signal was acquired with a TE cooled CCD detector. Initially, samples were treated with a chemical clean in 49.0 ~ 51.0 % hydrofluoric acid solution for 10 min to remove the contaminants on the surface and were flushed with the deionized water for 3 times to clean up the remaining chemicals. For each growth, samples were carefully bonded to an Inconel sample holder with indium solder to ensure a good thermal conductivity since SiC would not get enough heat with the radiation due to its wide band gap (~3.23 eV). Subsequently, the samples were degassed at 700 ˚C for 30 min under a vacuum below $1\times10^{-4}$ Torr to desorb water and other contaminants on the surface. After then, the substrates were within ± 1 nm roughness, as shown with the AFM image in Fig. S1(c).

For the deposition amount variation, the deposition amount were varied between 3 and 100 nm (3, 5, 7, 8, 9, 10, 25, 40, 70, 100 nm) in a plasma ion-coater below $1 \times 10^{-1}$ Torr. The deposition amount was controlled by varying the deposition time at a growth rate of 0.05 nm/s at the ionization current of 3 mA and the growth rate was calibrated by the X-ray measurement. The surface morphologies of the samples after Au deposition are presented in Fig. S2, and the corresponding values are summarized in Table S1. The surface morphologies appeared relatively smooth within a modulation of several nanometers, indicating the nanostructures only formed after annealing. Samples were systematically annealed by a halogen lamp and the substrate temperature ($T_{sub}$) was controlled by a computer-operated recipe at a ramping rate of 2 ˚C/s under $1\times10^{-4}$ Torr. After reaching each target $T_{sub}$, a dwelling of 450 s was given to ensure the uniformity of the Au nanostructures. For the systematic experiment, the other two parameters such as annealing temperature and dwelling time were fixed at 800 ℃ for 450 s while varying dwelling time. For the annealing temperature variation, similarly, deposition amount and dwelling time were fixed at 8 nm for 450 s and the temperatures were varied between 400 and 1000 ˚C. To investigate the dwelling

time effect, the dwelling durations were varied between 150 and 3600 s while fixing the deposition amount and annealing temperature at 8 nm and 800 ˚C. With the termination of each growth, the $T_{sub}$ was immediately quenched down to the ambient to minimize the Ostwald-ripening.[24,25]

For small area characterization, an atomic force microscope (AFM) under a non-contact (tapping) mode was utilized and a scanning electron microscopy (SEM) was employed for large area analysis. The cantilevers (NSC16/AIBS, μmasch) for AFM scans were back-side coated with ~ 30 nm Al to enhance the reflection by a factor of ~ 2.5 and the spring constant and resonant frequency of tips were ~ 42 N/m and ~ 330 kHz with a radius of curvature of less than 10 nm. To reduce the tip effect and improve the consistency of the analysis, the same type of tips from a single batch were used. For the analysis of the acquired data, XEI software (Park Systems) was utilized in terms of AFM top- and side-views, Fourier filter transform (FFT) power spectra, cross-sectional surface line-profiles. The FFT power spectrum shows height distribution and directionally by converting the height information from the spatial domain to the frequency domain using the Fourier filter transform. The surface area ratio (SAR) was given by $SAR = \frac{(S_T - S_G)}{S_T} \times 100$ [%] where $S_G$ is the geometric area (x × y), $S_T$ is the topologic area (x × y × z). The elemental analysis was carried out with an energy-dispersive x-ray spectroscopy (EDS) system with the spectral mode (Thermo Fisher Noran System 7) under vacuum (over $2\times10^{-4}$ Torr).

## III. Results and discussion

Figures 1 and 2 show the evolution of self-assembled Au NPs by the variation of deposition amounts between 3 and 25 nm on 4H-SiC (0001). In general, at relatively low deposition amounts, round-dome shaped droplets (DPs) were fabricated and the size of Au DPs was gradually expanded. With the increased deposition amounts, the dome shaped DPs gradually evolved into larger hexagonal nano-crystals. Meanwhile, the density was significantly

dropped. As clearly shown in Figs. 1 and 2, the self-assembled Au nanoparticles (3-D islands) rather than films were fabricated at each deposition amount after the annealing, which can be described based on the Volmer-Weber growth model. Given that, the bonding energy between Au adatoms ($E_{Au}$) is relatively stronger than that between Au adatoms and Si and C atoms ($E_I$) ($E_{Au} > E_I$), the Au adatoms can spontaneously diffuse and form the nuclei at relatively low energy sites. With the sufficient thermal energy at 800 °C, favorable diffusion can be expected and the Au nuclei can keep absorbing nearby adatoms with the stronger bonding energy ($E_{Au} > E_I$) to form 3-D islands until reaching an equilibrium, which can be similarly witnessed with Ag nanoparticles on SiC[26] and Au nanoparticles on $MgB_2$.[27] In the meantime, with the increased deposition amounts, additional Au atoms are available within the absorption boundary and in turn can result in the increased size of islands. Due to the merging tendency of larger islands, the density can be gradually reduced until reaching the balance in the thermodynamic system. More specifically, initially, with the 3 nm Au deposition, small round-dome shaped DPs were fabricated with the highly packed density as shown in Fig. 1(a) and 1(a-2) and between 3 and 8 nm deposition amounts, the gradual size increase of Au DPs with the sharp decrease in density was observed as clearly shown in Fig. 1 and 2. At 9 nm, the shape of Au NPs began to transform to polyhedral Au nano-crystals as evidenced by the slender facet formation on the AFM side-view in Fig. 2(b-1) and with additional depositions of 10 and 25 nm, the hexagonal shape much more evidently appeared as clearly shown in Fig. 2(c) and 2(d). The self-assembled Au hexagonal nano-crystals on 4H-SiC (0001) with the Au deposition amounts of (a) 9.5, (b) 10 and (c) 25 nm can also be witnessed with the 3-D side-view AFM images in Fig. S3. The shape transformation of Au NPs can be guided by the underlying substrate crystal configuration depending on the growth conditions such that the final shape of NPs under an equilibrium can balance the surface energy for a certain volume.[28] Generally, when the surface energy is isotropic for a given volume, spherical (dome) shape is preferred in order to minimize the surface energy. As the volume of nanostructures becomes

larger and reaches the critical volume, the isotropic surface energy along various directions cannot be sustained, and the local breakage of the isotropy of the surface energy can lead to the formation of additional surfaces along the lower energy directions.[23, 28] Such that, up to 8 nm deposition amount, the resulting configuration was in the form of round-dome shape, however, above 9 nm, the Au NPs can absorb more Au adatoms with the increased deposition amount and the size increase by merging nearby droplets, the surface energy of Au NPs can become anisotropic and thus the resulting configuration can be the hexagonal nano-crystals and the truncation (or facet formation) can be obtained as clearly seen in Fig. S3 and S4. The surface morphology evolution of Au NPs can also be witnessed with the Fourier filter transform (FFT) power spectra, as shown in the insets of Fig. 1(a-1) - 1(c-1) and Fig. 2(a-3) - 2(d-3). At 3 nm, the bright spot in a symmetric round shape occupied almost 90 % area due to a broad distribution of droplet height. With the deposition amount increase, the spot size drastically shrunk due to the reduction in the height distribution and density reduction and finally became asymmetric because of the appearance of the polyhedron shape of Au nano-crystals. Fig. 3 shows the overall deposition amount variations between 3 and 100 nm and the evolution of self-assembled Au NPs on 4H-SiC (0001) and the summary of size, density and $R_{RMS}$. The corresponding values are provided in Table SII. Top-view and 3-D side-view AFM images between 25 – 100 nm deposition amounts are provided in Fig. S5 and S6. As discussed, above 9 nm, the formation of Au nano-crystals with clear facets appeared and kept evolving in larger crystals with the density reduction as shown in Fig. 3(e) – 3(j). In addition to the shape transition of NPs, when the deposition amounts were systematically varied between 3 and 100 nm, the size of the Au nanostructures kept radically increasing by 105 times with the AH from ~ 8.7 at 3 nm to ~ 914.8 nm at 100 nm and 67 times with the LD from ~ 45.6 to ~ 3066.7 nm as a function of the deposition amount as shown in Fig. 3(o). The aspect ratio (AH : LD) was ~ 1 : 5 with the 3 nm Au deposition and that with 100 nm Au deposition was ~ 1 : 3, suggesting a preferential vertical growth. Correspondingly, the AD

was rapidly decreased by ~ 5 orders from ~ $1.18 \times 10^{11}$ to ~ $7.6 \times 10^{6}$ $cm^{-2}$ as a compensation of the size expansion as shown in Fig. 3(p). With the increased size of NPs, the $R_{RMS}$ was gradually increased from 2.1 to 304 nm between 3 and 100 nm as shown in Fig. 3(q). The elemental analysis of corresponding samples are presented by the Energy-dispersive X-ray spectroscopy (EDS) phase maps and spectra in Fig. 4. Fig. 4(a) shows the SEM image of the sample with 25 nm Au deposition and the combined phase map of Au and Si in Fig. 4(b) clearly matches with the SEM image. The separate maps of Si and Au phase in Fig. 4(c) and 4(d) also clearly support the formation of Au NPs. The Au count line profiles and spectra on the locations with/without Au droplets are shown with Fig. 4(e) - 4(g), acquired from the lines and boxes in the inset of the SEM image. In Fig. 4(e), the high count of Au was clearly witnessed along the line-profile (W) while only Si was observed with the profile (WO). Similarly, this is also observed with the existence of the Au Mα1 peak in the spectrum from the NP region in Fig. 4(f) while only Si Kα and C Kα were observed in Fig. 4(g). This clearly indicates that the fabrication of Au nanoparticles was based on the Volmer-Weber growth model without the formation of wetting layer in between the Au NPs. The evolution of the Au Mα1 peak at 2.123KeV as function of deposition amount was clearly observed in Fig. 4(h) from 3 to 100 nm deposition amounts variation, and the corresponding full range spectra are shown in Fig. S9. For instance, the Au Mα1 count with 3 nm was ~ 300 and gradually increased and reached ~ 2400 with 100 nm. After the excitation of electrons to N orbit, the electrons spontaneously release energy to relax to M orbit, which results in the Mα1 peak and thus, the increased deposition amount can directly enhance the count of Au Mα1 peak. Fig. S7 presents the 3-D side- and top-views of EDS maps with the 100 nm Au deposition and Fig. S8 shows the full range EDS spectra of the samples with (a) 3 and (b) 100 nm Au deposition amounts. In summary, the self-assembled Au NPs were successfully fabricated on 4H-SiC (0001) and the Au NPs very sensitively responded to the variation of the deposition amounts, which led to the drastic evolution in size and density as well as the configuration being

provided with the $E_{Au} > E_I$.[26-27] When the binding energy between adatoms is stronger, but not strong enough to maintain the 3-D structure, the coalescence growth model can take the dominance with the increased deposition amount such that the layer formation of Au film can follow immediately after a few nanometer depositions. For instance, Au NPs can be fabricated with less than 5 nm Au depostion on Si (111)[29], glass,[30] $SiO_2$,[31] and polymeric substrates (polystyrene and poly methyl methacrylate)[31] but with further increased deposition amounts, the merging of Au nanostructures gradually occurred and finally coalesced into a layer based on the Coalescence growth model. However, on SiC, the size of self-assembled Au NPs was gradually increased with the facet formation even up to 100 nm deposition amount. As another aspect, the Au NPs on 4H-SiC (0001) for a given deposition amount showed relatively much smaller size distribution (i.e. at 3 nm, the AH: ~ 8.7 nm and LD: ~ 45.6) with a highly packed density as compared with the counterparts on GaAs[33-35] and Si,[29,36] which can likely be due to the much higher diffusion barrier caused by the higher surface roughness of the SiC.[37]

Figure 5 and 6 show the configuration evolution of self-assembled Au nanostructures by the control of annealing temperatures between 400 and 1000 °C with a fixed deposition amount of 8 nm on 4H-SiC (0001). Generally, two distinctive confugrations of Au nansostructures were observed with the systematical variation of annealing temperatures: Au nano-mounds between 400 and 700 °C (Regime I) and round-dome shaped DPs between 750 and 1000 °C (Regime II). Detailed evolution process of irregular Au nano-mounds with a smaller increment of annealing temperatures between 400 and 700 °C is shown with top- and side- view AFM images in Fig. S10 – S11. The formation of irregular Au nano-mounds can be described with the diffusion limited aggregation (DLA) growth model in conjunction of the theromodynamic diffusion theory.[22,23] The diffusion length ($l_D$) can be expressed as $l_D = \sqrt{D_S t}$, where $D_S$ is the surface diffusion coefficient and $t$ is the residence time of Au atoms. Herein, the $D_S$ can be given by $D_S = D_0 e^{\frac{-E_A}{kT}}$ and the $E_A$ is the interface energy

between Au and substrate and the $k$ is Boltzmann constant.[38] By combining both equations, the diffusion length ($l_D$) can be expressed as a direct function of temperature such that the $l_D$ can be directly controlled by the variation of temperature. In the meantime, the vacancy of atoms in Au film can occur at an elevated temperature, whose concentration can gradually increase along with the increased thermal energy. At a critial thermal energy or concentration of vacancy, it can turn into the formation of voids according to the DLA model.[21,22,39] The voids can perforate the Au film and create punctures when the density of voids reaches a critical value, which gradually expand owing to the enhanced Au adatoms diffusion.[40] Finally, Au film branches into isolated Au mounds due to the Rayleigh instability[41] and in turn results in the formation of isolated irregular Au mounds.[22] Such that, at 400 °C as clearly seen in Fig. 5(a), the resulting geometry was connected Au wiggily branch structures with the height of ~ 20 nm due to the limited diffussion and along with the increased temperature up to 700 °C, the enhanced diffussion gradually led the separation of Au wiggily structures into the isolated nano-mounds as described above and reached height of ~ 40 nm as clearly shown in Fig. 5, S9 and S10. The formation of irregular nano-mounds can also be obseved with the Co[42] and Ni NPs.[43] The morphologic changes can also be described by the SAR and $R_{RMS}$ in Fig. 7(g) and both values in phase I were generally lower than the phase II but were gradually increased along with the increased annealing temperature; 9 – 17 nm for the $R_{RMS}$ and 15 – 30 % for the SAR as shwon in Fig. 7(c). As the AT was further increased to 750 - 1000 °C, the self-aseembled round-dome shaped Au droplets (DPs) were formed owing to the sufficient diffusion energy being provided with the stronger binding energy ($E_{Au} > E_I$) and generaly, the size of the Au DPs were gradually increased while the density kept decreasing. The top-views and line-profiles of DPs are provided in Figs. 6 and S11. The size and density are summarized in the Fig. 7(a) and 7(b) and also specific values are listed in Table SIII. The enhanced diffusion can lead to the increased size of DPs and the larger DPs with increased absorption boundary tend to absorb or merge nearby smaller DPs and thus the density derease can occur

until reaching in equlibrium. For example, during the annealing temperature variations between 750 and 900 °C as shown in Fig. 7(a) – 7(b), the AH was increased by 1.4 times from 51.9 to 70.5 nm, and the LD was increased by 1.1 times from 161.9 to 174.8 nm but the AD was decreased by 34.9 % from $6.57 \times 10^9$ to $4.28 \times 10^9$ $cm^{-2}$. The size increase was also clearly observed in both SAR and $R_{RMS}$ in Fig. 7(c). At 1000 °C, the size, SAR and $R_{RMS}$ of DPs were sharply decreased, which can be resulted from the Au evaporation caused by the elevated temperature. As well known, the melting point of the bulk of Au is 1064 °C, whereas, the melting point of the Au NPs can be lower due to the variation of the Au vapor pressure saturation, as witnessed on MgO, $SrTiO_3$, and $Al_2O_3$.[44] In brief, along with the AT variation, the self-assembled Au nanostructures exhibited two distinctive configurations of irregular Au mounds (Regime I) and round-dome shape DPs (Regime II). The irregular Au mounds were formed due to the diffusion limited aggregation at relative low annealing temperatures between 400 and 700 °C and between 750 and 900 °C, the round-dome shape DPs were fabricated due to the stronger binding energy ($E_{Au} > E_I$) and sufficeint diffusion energy and the size of DPs was gradually increased while the density was decresed. The inverse relationship between the size and density of DPs can also be observed on other substrates such as Si[45,46] and Sapphire.[47]

Fig. 8 shows the map of self-assembled Au nanostructure fabrication with the variation of annealing temperature as a function of deposition amount. Depending on the fabrication condition, the overall evolution is divided into three seasons: nano-mound, droplets and nano-crystals. In the nano-mound season as indicated with No. 1 - 2, Au nanostructures nucleate but due to the low thermal energy or limited diffusion, the Au mounds were formed based on the diffusion limited aggregation model between 400 and 700 °C. In the droplet season as indicated with No. 3 - 6, due to the enhanced thermal energy, the round-dome shaped Au droplets were fabricated at above 750 °C being provided with the stronger binding energy ($E_{Au} > E_I$). In the nano-crystal season indicated with No. 7 - 10, the

self-assembled Au hexagonal nano-crystals were formed due to the local breakage of the isotropy of the surface energy caused by the larger volume of nanostructures, which occurred at ~ 9 nm deposition. The $R_{RMS}$ of related samples are shown in Fig. 8(a) and 8(b). Depending on the deposition amount, the $R_{RMS}$ is gradually increased along with the size evolution of nanostructures. Depending on the annealing temperature, the $R_{RMS}$ is also gradually increased, however, at 900 °C, it is decreased potentially due to the the Au evaporation.

Fig. 9 shows the evolution of the self-assembled Au DPs by the variation of the dwelling time between 150 and 3600 s with 8 nm of Au deposition at 800 °C. The 3-D side-views are provided in Fig. S13. As summarized in Fig. 9(h) – 9(i), the size of self-assembled Au DPs gradually became larger with the increased dwelling time while the density kept decreasing. The annealing duration related evolution of nanoparticles can be described based on the Ostwald-ripening,[24] in which the average radius of Au DPs *(<R(t)>)* can be expressed as $< R(t) >^4 - < R_0 >^4 = \frac{8N_0 D_S \gamma \Omega^2}{45kT \ln(3)} t$, where $<R_0>$ is the initial radius of Au DP, and Ω is the atomic volume.[25,38] The density of nucleation sites ($N_0$) and the interface energy ($\gamma$) can be constant and thus, the final size of Au DPs (<R>) can be determined depending on the dwelling time variation and based on the equation, the <R> can be increased along with the increased dwelling time. For example, the LD was ~ 157 nm with 150 s annealing and was increased to ~ 180 nm with 3600 s and similarly the AH of DPs was 62.2 nm with 150 s annealing and was increased to 69 nm with 3600 s. Meanwhile the AD was $4.76 \times 10^9$ /cm$^2$ with 150 s and gradually decreased to $3.71 \times 10^9$ /cm$^2$ with 3600 s. Likewise, the SAR and $R_{RMS}$ also showed gradual increase, as shown in Fig. 9(j). The change of size and density rather rapidly occurred at earlier stage as clearly seen with the sharper slopes of the plots up to 900 s and as the time is further increased, the change became mild with the slender slope. With the increased annealing time, the critical size $<R_C>$ should reach and naturally further increased time can only have insignificant effect. In this experiment, a relative slow ramping (2 ˚C /s) was utilized to ensure the proper thermal conduction and thus the ripening could

have occurred during the ramping up. The mild size and density change as compared to the temperature and deposition amount variation can also be observed with the similar FFT size and patterns. Nevertheless, it is worthwhile to observe the size and density evolution of DPs depending on the time. Meanwhile, as shown in Fig. 9(f) and 9(g), the slightly increase in deposition amount resulted in the formation of hexagonal Au nano-crystals and the small decrement of annealing temperature showed the fabrication of Au nano-mounds. In particular, we can conclude that the variation in dwelling time had nearly no effect on the shape of Au NPs as the configuration was more strongly dependent on the annealing temperature and deposition amount for a fixed condition as discussed above.

## IV. Conclusions

In summary, systematic approaches to control the size, density, and configuration of self-assembled Au nanostructures on 4H-SiC (0001) were investigated through the variation of deposition amount, annealing temperature and dwelling time. With the deposition amount variation, the self-assembled Au NPs of round-dome shape were successfully fabricated based on the Volmer-Weber growth model and evolved into hexagonal Au nano-crystals. Au NPs very sensitively responded to the deposition amount variation and resulted in the drastic size and density evolution along with the configuration transition. Depending on the annealing temperature variation, two distinctive configurations of Au nanostructures, Au nano-mounds (Regime I) and round-dome shaped Au droplets (Regime II), were fabricated based on the diffusion limited aggregation and thermodynamic theories. Depending on the dewelling time, the size and density evolution of dome shaped Au droplets were discussed based on the Ostwald-ripening theory.

## Acknowledgements

Financial supports from the National Research Foundation of Korea (no. 2011-0030079 and 2016R1A1A1A05005009), the National Science Foundation of USA (no. US/NSF/DMR1309989) and in part by the research grant of Kwangwoon University in 2016 are gratefully acknowledged.

**References**


1 M. Valden, X. Lai, D. W. Goodman, *Science* 1998, **281**, 1647-1650.

2 M. J. Walsh, K. Yoshida, A. Kuwabara, M. L. Pay, P. L. Gai, E. D. Boyes, *Nano Lett*. 2012, **12**, 2027-2031.

3 S.-S. Kim, Y.-R. Kim, T. D. Chung, B.-H. Sohn, *Adv*. *Funct*. *Mater*. 2014, **24**, 2764–2771.

4 R. Kraya, L. Y. Kraya, D. A. Bonnell, *Nano Lett*. 2010, **10**, 1224–1228.

5 T. Lohmuller, S. Triffo, G. P. O'Donoghue, Q. Xu, M. P. Coyle, J. T. Groves, *Nano Lett*. 2011, **11**, 4912–4918.

6 P. Ginzburg, N. Berkovitch, A. Nevet, I. Shor, *Nano Lett*. 2011, **11**, 2329–2333.

7 G. V. Naik, V. M. Shalaev, A. Boltasseva, *Adv*. *Mater*. 2013, **25**, 3264–3294.

8 S. H. Mirsadeghi, J. F. Young, *Nano Lett*. 2014, **14**, 5004−5009.

9 E. Thimsen, F. L. Formal, M. Gratzel, S. C. Warren, *Nano Lett*. 2011, **11**, 35–43.

10 N. P. Dasgupta, J. Sun, C. Liu, S. Brittman, S. C. Andrews, J. Lim, H. Gao, R. Yan, P. Yang, *Adv*. *Mater*. 2014, **26**, 2137–2184.

11 M. Kolíbal, T. Vystavěl, P. Varga, T. Šikola, *Nano Lett*. 2014, **14**, 1756−1761.

12 V. Schmidt, S. Senz, U. Go1sele, *Nano Lett*. 2005, **5**, 931-935.

13 Vreede, L. J. D.; Berg, A. V. D.; Eijkel, J. C. T. Nanopore Fabrication by Heating Au Particles on Ceramic Substrates. *Nano Lett*. 2015, **15**, 727-731.

14 James, T.; Kalinin, Y. V.; Chan, C.-C.; Randhawa, J. S.; Gaevski, M.; Gracias, D. H. Voltage-Gated Ion Transport through Semiconducting Conical Nanopores Formed by Metal Nanoparticle-Assisted Plasma Etching. *Nano Lett*. 2012, **12**, 3437-3442.

15 E. Velez-Fort, C. Mathieu, E. Pallecchi, M. Pigneur, M. G. Silly, R. Belkhou, M. Marangolo, A. Shukla, F. Sirotti, *ASC Nano* 2012, **6**, 10893–10900.

16 H. Frenzel, A. Lajn, H. V. Wenckstern, M. Lorenz, F. Schein, Z. Zhang, M. Grundmann, *Adv*. *Mater*. 2010, **22**, 5332–5349.

17 C. Huh, K.-H. Kim, B. K. Kim, W. Kim, H. Ko, C.-J. Choi, G. Y. Sung, *Adv*. *Mater*. 2010, **22**, 5058–5062.

18 J. D. Caldwell, O. J. Glembocki, Y. Francescato, N. Sharac, V. Giannini, F. J. Bezares, J. P. Long, J. C. Owrutsky, I. Vurgaftman, J. G. Tischler, V. D. Wheeler, N. D. Bassim, L. M. Shirey, R. Kasica, S. A. Maier, *Nano Lett*. 2013, **13**, 3690−3697.

19 T. Low, P. Avouris, *ASC Nano* 2014, **6**, 1086–1101.

20 D. Tsivion, E. Joselevich, *Nano Lett*. 2013, **13**, 5491−5496.

21 M.-Y. Li, Q. Zhang, P. Pandey, M. Sui, E.-S. Kim, J. Lee, *Sci. Rep.* **2015**, *5*, 13954.

22 J.-Y. Kwon, T.-S. Yoon, K.-B. Kim, S.-H. Min, *J*. *Appl*. *Phys*. 2003, **93**, 3270-3278.

23 T. A. Witten, L. M. Sander, *Phys*. *Rev*. *B* 1983, **27**, 5686-5697.

24 J. H. Yao, K. R. Elder, H. Guo, M. Grant, *Phys*. *Rev*. *B* 1993, **47**, 14110-14125.

25 F. Ruffino, M. G. Grimaldi, *J*. *Appl*. *Phys*. 2010, **107**, 104321(1)-104321(9).

26 F. Ruffino, M. G. Grimaldi, *J. Appl. Phys.* 2011, **110**, 044311.

27 A.V. Pogrebnyakov, J.M. Redwing, S. Raghavan, V. Vaithyanathan, D.G. Schlom, S.Y. Xu, Q. Li, D. A. Tenne, A. Soukiassian, X. X. Xi, M. D. Johannes, D. Kasinathan, W. E. Pickett, J. S. Wu, J. C. H. Spence, *Phys. Rev. Lett.* 2004, **93** 147006(1)-147006(4).

28 T. K. Sau, A. L. Rogach, *Adv*. *Mater*. 2010, **22**, 1781–1804.

29 M.-Y. Li, M. Sui, E.-S. Kim, J. Lee, *Cryst*. *Growth Des*. 2014, **14**, 1128−1134.

30 D. Gaspar, A. C. Pimentel, T. Mateus, J. P. Leitao, J. Soares, B. P. Falcao, A. Araujo, A. Vicente, S. A. Filonovich, H. Aguas, R. Martins, I. Ferreira, *Sci*. *Rep*. 2013, **3**, 1469(1)-1469(5).

31 S. M. Tabakman, Z. Chen, H. S. Casalongue, H. Wang, H. Dai, *Small* 2011, **7**, 499–505.

32 F. Ruffino, V. Torrisi, G. Marletta, M.G. Grimaldi, *Appl*. *Phys*. *A* 2011, **103**, 939–949.

33 M.-Y. Li, M. Sui, E.-S. Kim, J. Lee, *Jpn*. *J*. *Appl*. *Phys*. 2014, **53**, 095502(1)- 095502(6).

34 S.Y. Sayed, B. Daly, J. M. Buriak, *J*. *Phys*. *Chem*. *C* 2008, **112**, 12291–12298.

35 M. Sui, M.-Y. Li, E.-S. Kim, J. Lee, *J*. *Appl*. *Cryst*. 2014, **47**, 1-6.

36 L. K. Ono, F. Behafarid, B. R. Cuenya, *ACS Nano* 2013, **7**, 10327–10334.

37 M.-Y. Li, M. Sui, E.-S. Kim, J. Lee, *J. Appl. Phys*. 2014, **116**, 084301(1)-084301(9).

38 F. Ruffino, A. Canino, M. G. Grimaldi, F. Giannazzo, C. Bongiorno, F. Roccaforte, V. Raineri, *J. Appl. Phys*. 2007, **101**, 064306(1)- 064306(7).

39 W. Lu, K. Komvopoulos, *J. Appl. Phys*. 2000, **76**, 3206-3208.

40 F. Ruffino, M.G. Grimaldi, *Thin Solid Films* 2013, **536**, 99–110.

41 A. M. Glaeser, *Interface Sci*. 2001, **9**, 65–82.

42 J. Lian, L. Wang, X. Sun, Q. Yu, R. C. Ewing, *Nano Lett*. 2006, **6**, 1047-1052.

43 L. Kondic, *Phys. Rev. E* 2009, **79**, 026302(1)-026302(7).

44 G. Meng, T. Yanagida, M. Kanai, M. Suzuki, K. Nagashima, B. Xu, F. Zhuge, *Phys. Rev. E* 2013, **87**, 012405(1)-012405(7).

45 M. Sui, M.-Y. Li, E.-S. Kim, J. Lee *Nanoscale Res. Lett*. 2013, **8**, 525(1)- 525(8).

46 F. Ruffino, A. Canino, M. G. Grimaldi, F. Giannazzo, F. Roccaforte, V. Raineri, *J. Appl. Phys*. 2008, **104**, 024310(1)- 024310(7).

47 C.-Y. Chen, J.-Y. Wang, F.-J. Tsai, Y.-C. Lu, Y.-W. Kiang, C. C. Yang, *Opt. Express* 2009, **17**, 14186(1)-14186(13).

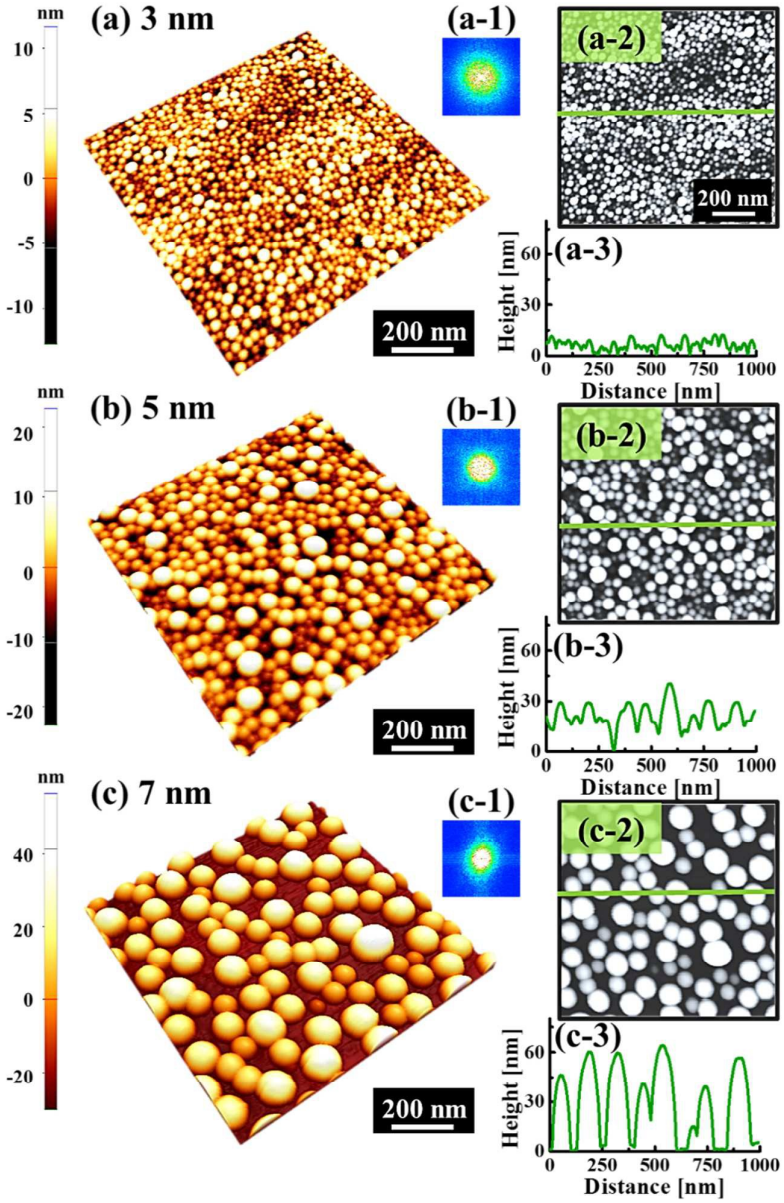


**Fig. 1** Self-assembled round-dome shaped Au droplets on 4H-SiC (0001) with a variation of Au deposition amounts between 3 and 7 nm. Au droplets were fabricated with a fixed annealing temperature at 800 °C and dwelling time for 450 s. (a) - (c) Atomic force microscopy (AFM) side-views of 1 × 1 $\mu m^2$. (a-1) – (c-1) Two dimensional (2-D) Fourier filter transform (FFT) power spectra. (a-2) – (c-2) Corresponding AFM top-views of 1 × 1 $\mu m^2$. (a-3) - (c-3) Corresponding cross-sectional line-profiles.

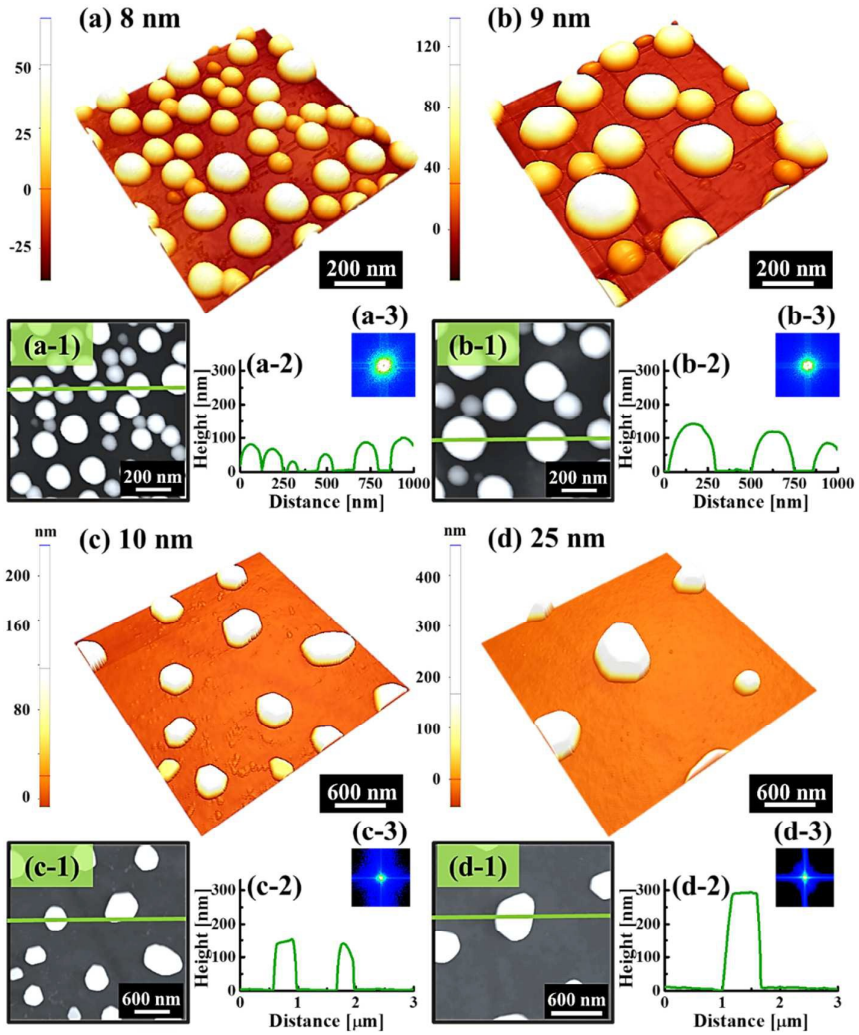


**Fig. 2** Shape transition of the self-assembled Au nanoparticles on 4H-SiC (0001) by the variation of deposition amounts between 8 and 25 nm under an identical growth condition (800 °C, 450 s). (a) - (b) AFM side-views of 1 × 1 μm$^2$ and (c) - (d) 3 × 3 μm$^2$. (a-1) - (b-1) AFM top-views of 1 × 1 μm$^2$ and (c-1) – (d-1) 3 × 3 μm$^2$. (a-2) – (d-2) Cross-sectional line-profiles acquired from the green lines drawn in (a-1) – (d-1). (a-3) – (b-3) 2-D FFT power spectra.

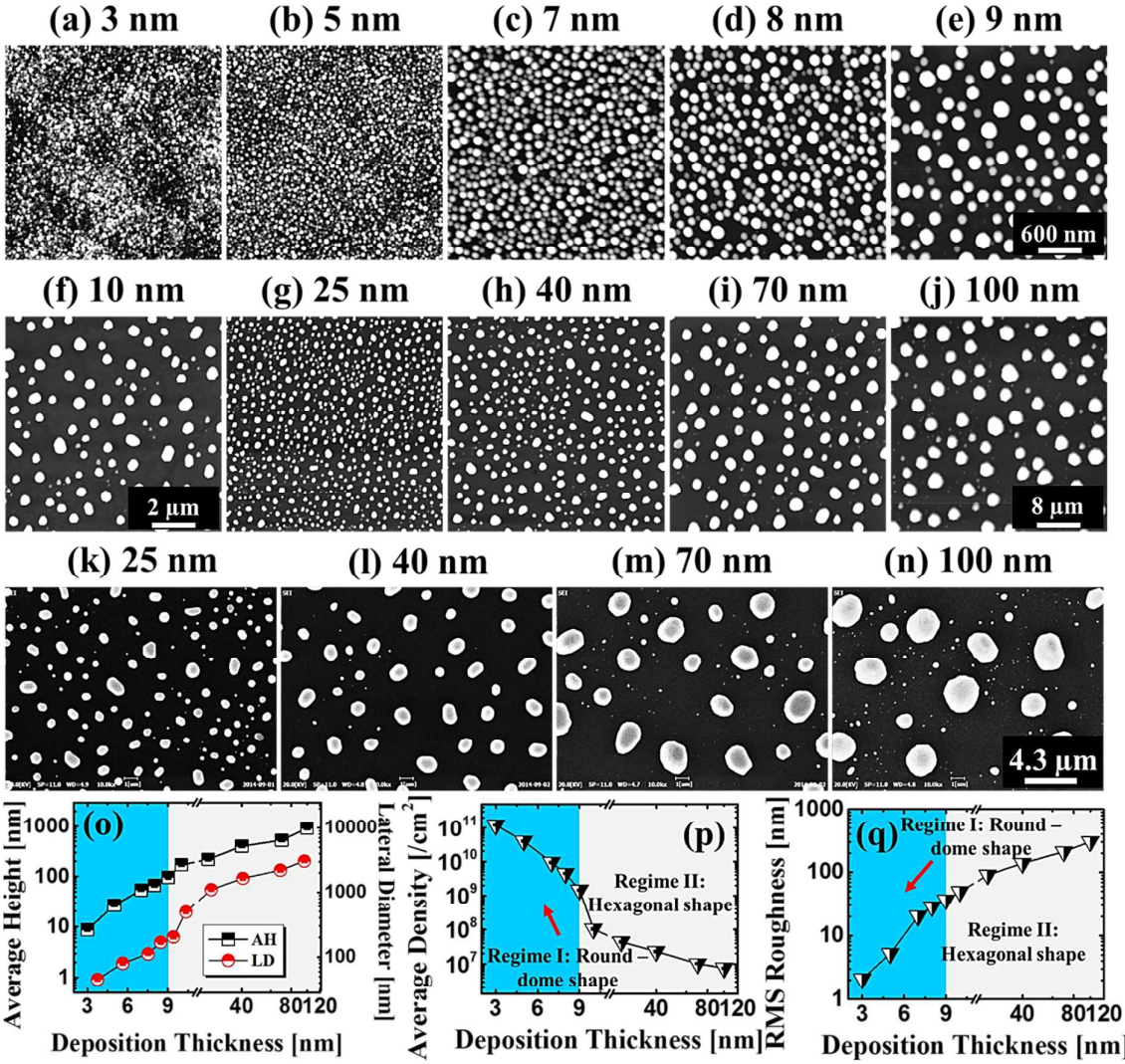


**Fig. 3** Evolution of self-assembled Au nanostructures by the variation of deposition amounts between 3 and 100 nm on 4H-SiC (0001) annealed at 800 ˚C for 450 s. (a) - (e) AFM top-views of 3 × 3 μm$^2$. (f) 10 × 10 μm$^2$. (g) - (j) 40 × 40 μm$^2$. (k) - (n) SEM images of 21.5 (x) × 16.13 (y) μm$^2$. (o) - (p) Plots of the average height (AH) and lateral diameter (LD), and average density (AD) of Au NPs with the error bars of ± 5 %. (q) Plot of the root mean squared roughness ($R_{RMS}$) of corresponding samples.

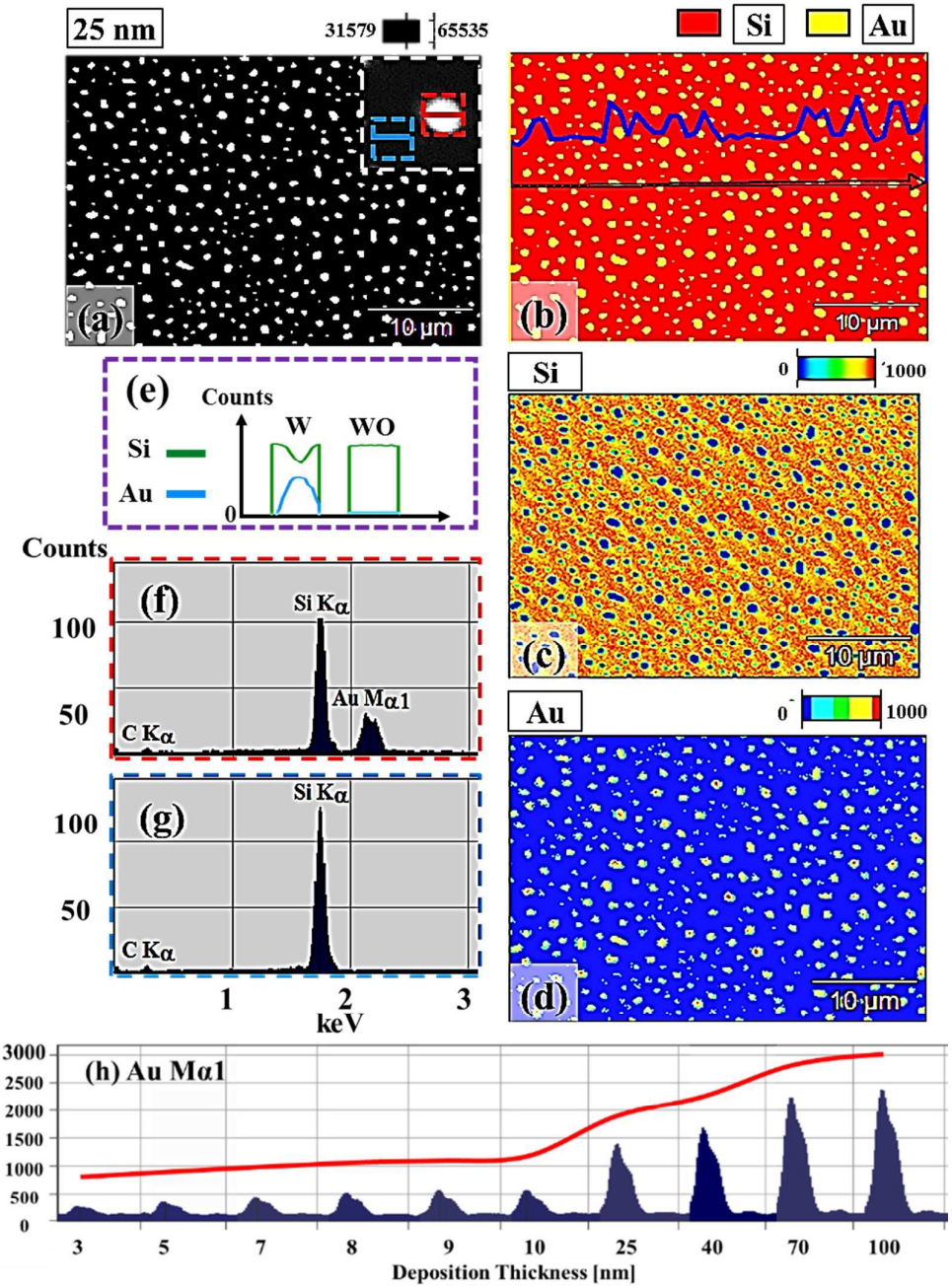


**Fig. 4** Energy-dispersive X-ray spectroscopy (EDS) elemental characterization of the Au NPs. (a) Scanning electron microscopy (SEM) image of the sample with 25 nm-thickness deposition. (b) EDS combined phase map of Si and Au. Line-profile shows the Au component along the arrow. (c) Si phase map. (d) Au phase map. (e) EDS local line-profiles of the element contents of Si (green) and Au (blue), which are acquired from the lines with (W) and without (WO) the Au NPs marked with red (W) and blue (WO) lines in (a). (f) - (g) EDS spectra of the locations indicated with red (f) and blue (g) boxes. (h) Evolution of Au Mα1 peaks at 2.123 keV with the increased deposition amounts between 3 and 100 nm.

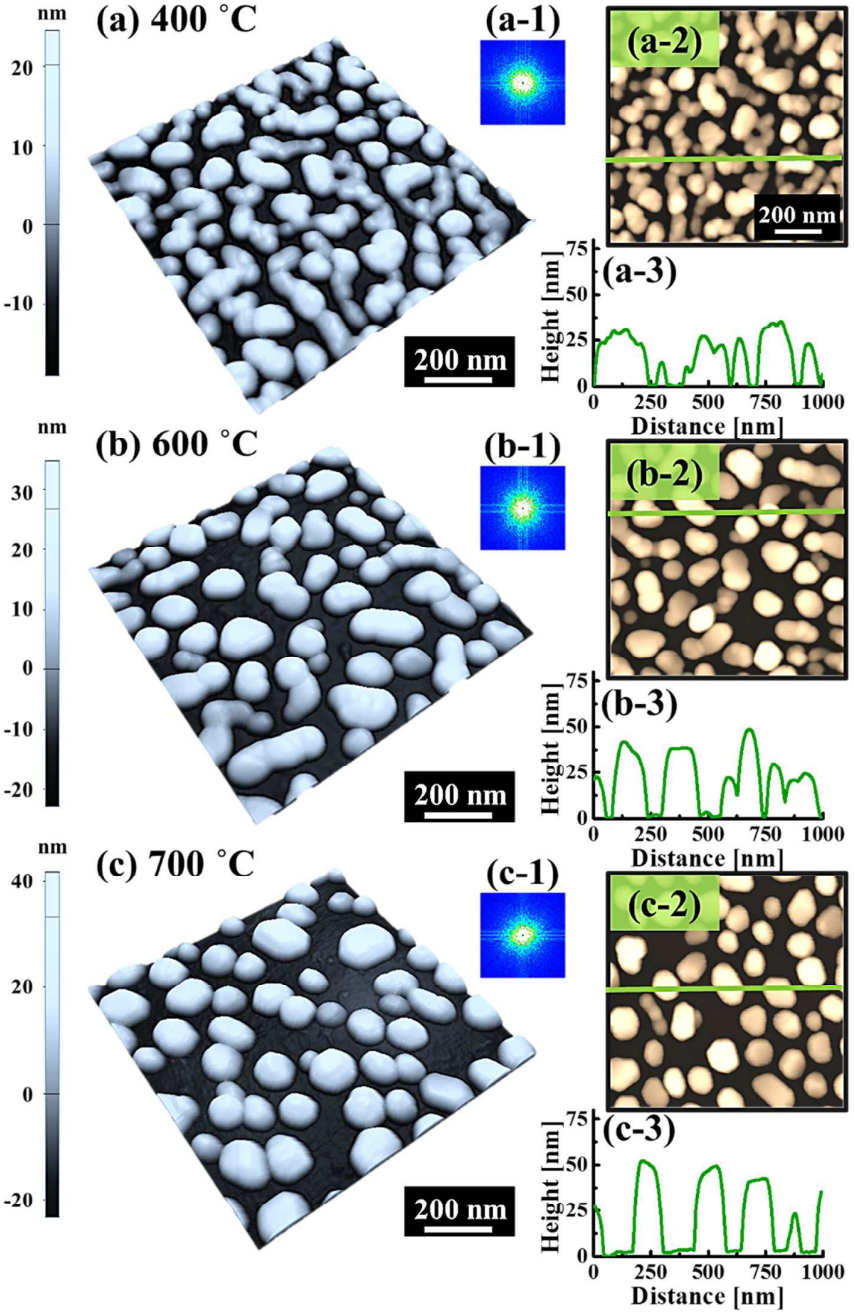


**Fig. 5** Evolution of Au nanostructures by the variation of annealing temperatures between 400 and 700 ˚C on 4H-SiC (0001). Each samples are fabricated with the fixed deposition amount of 8 nm and annealing duration for 450 s. (a) - (c) AFM side-views of 1 × 1 μm$^2$. (a-1) – (c-1) 2-D FFT power spectra. (a-2) – (c-2) AFM top-views of 1 × 1 μm$^2$. (a-3) - (c-3) Cross-sectional line-profiles.

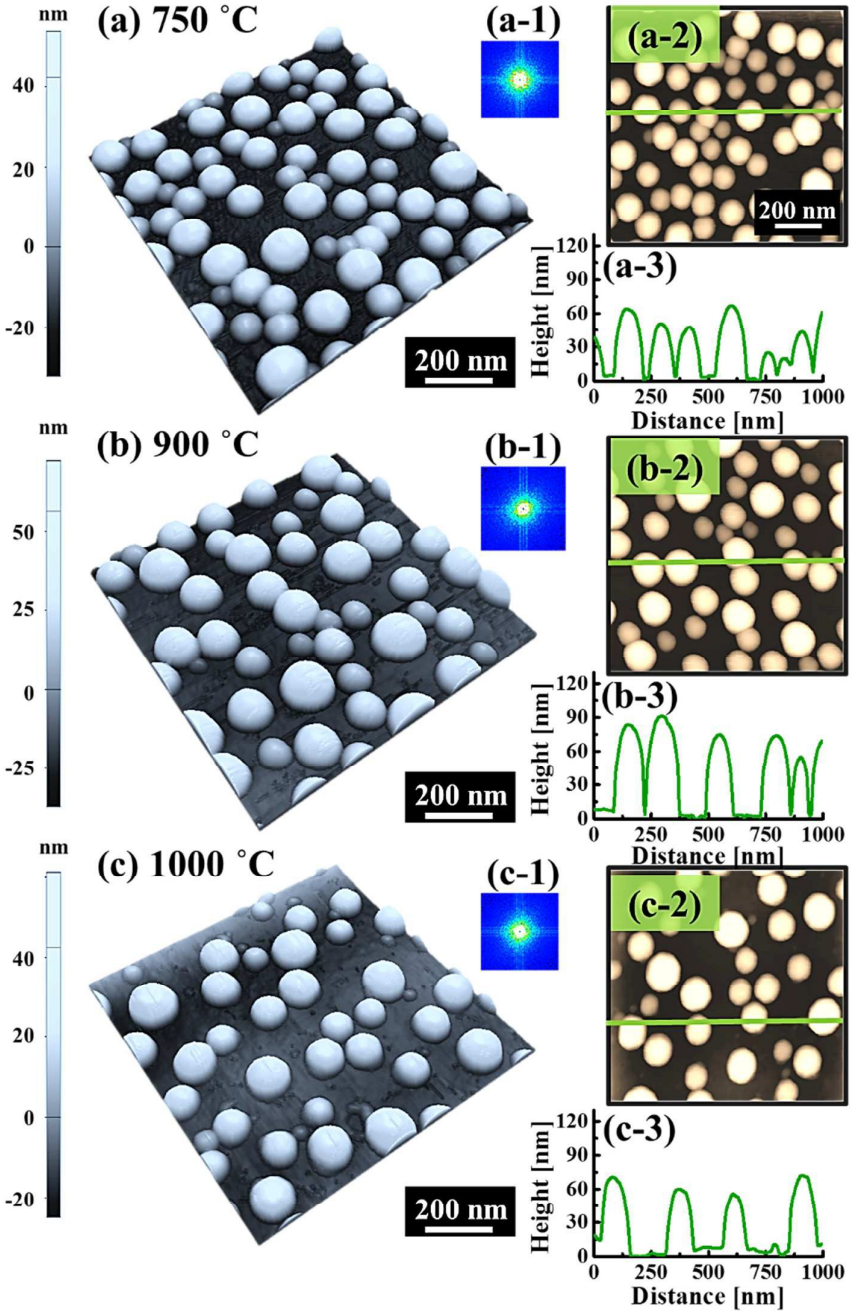


**Fig. 6** Fabrication of Au droplets with a variation of annealing temperatures between 750 and 1000 ˚C on 4H-SiC (0001) under a fixed condition (8 nm, 450 s). (a) - (c) AFM side-views of 1 × 1 μm$^2$. (a-1) – (c-1) 2-D FFT power spectra. (a-2) – (c-2) AFM top-views of 1 × 1 μm$^2$. (a-3) - (c-3) Cross-sectional line-profiles.

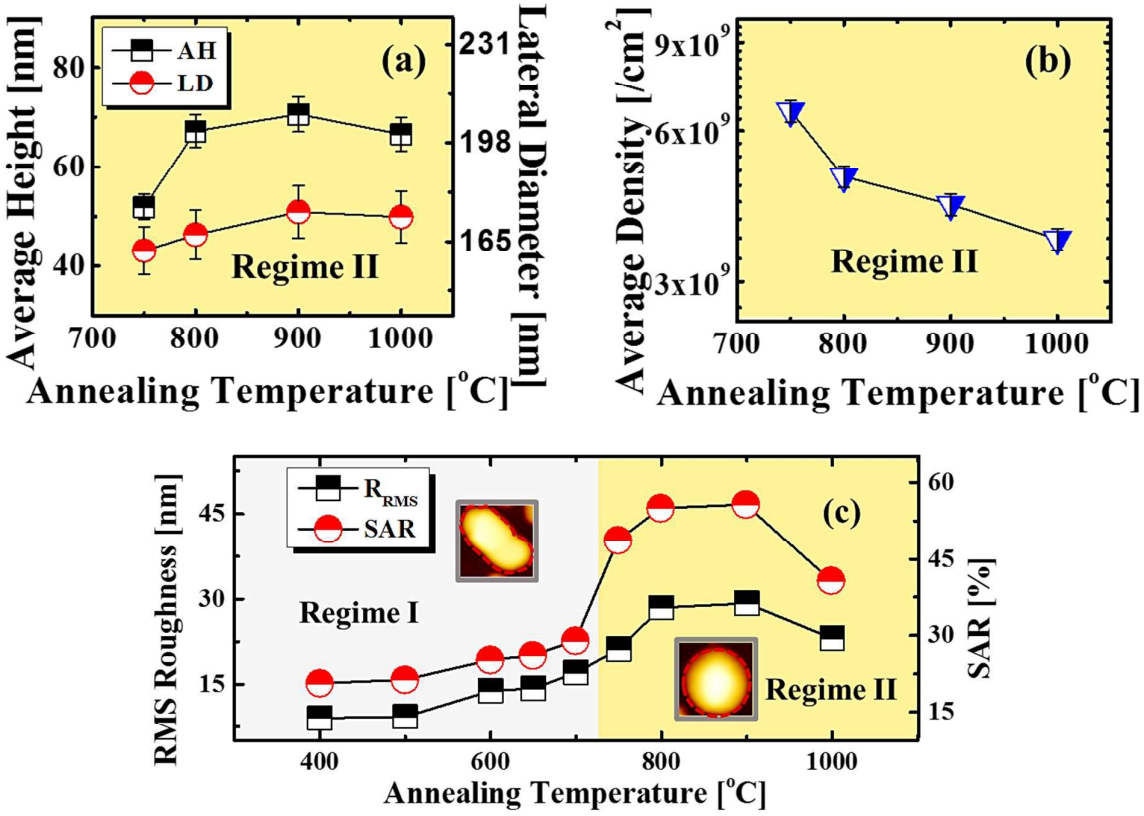


**Fig. 7** (a) - (b) Plots of the AH, LD and AD with the error bars of ± 5 %. (c) Plot of the $R_{RMS}$ and surface area ratio (SAR). The SAR is {(β - α) / β ] × 100 [%]}, with the surface area [α] of (x × y) and geometric area [β] of (x × y × z). (Insets) 150 × 150 $nm^2$.

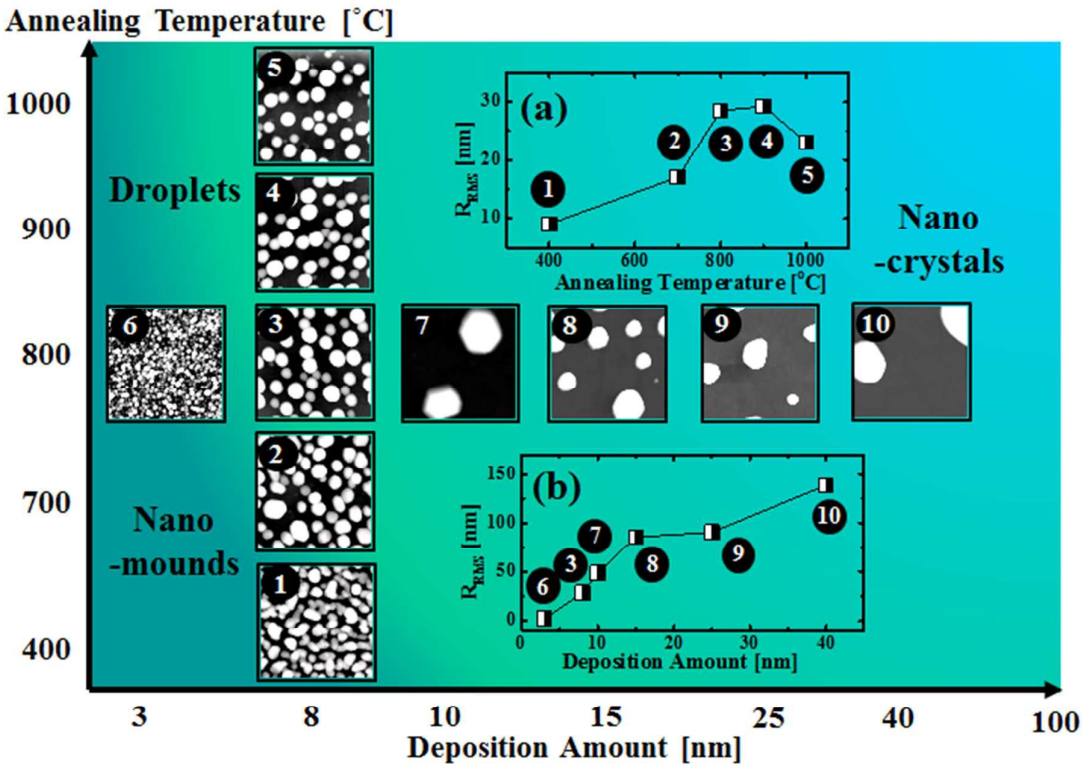


**Fig. 8** Map of the fabrication of self-assembled Au nanostructures by the variation of the deposition amounts versus annealing temperatures. (a) $R_{RMS}$ of the samples synthesized with 8 nm Au deposition at various annealing temperatures. (b) $R_{RMS}$ of the samples with various deposition amounts annealed at 800 °C for 450 s. (Insets) 1 × 1 μm$^2$ in 1 - 7 and 3 × 3 μm$^2$ in 8 - 10.

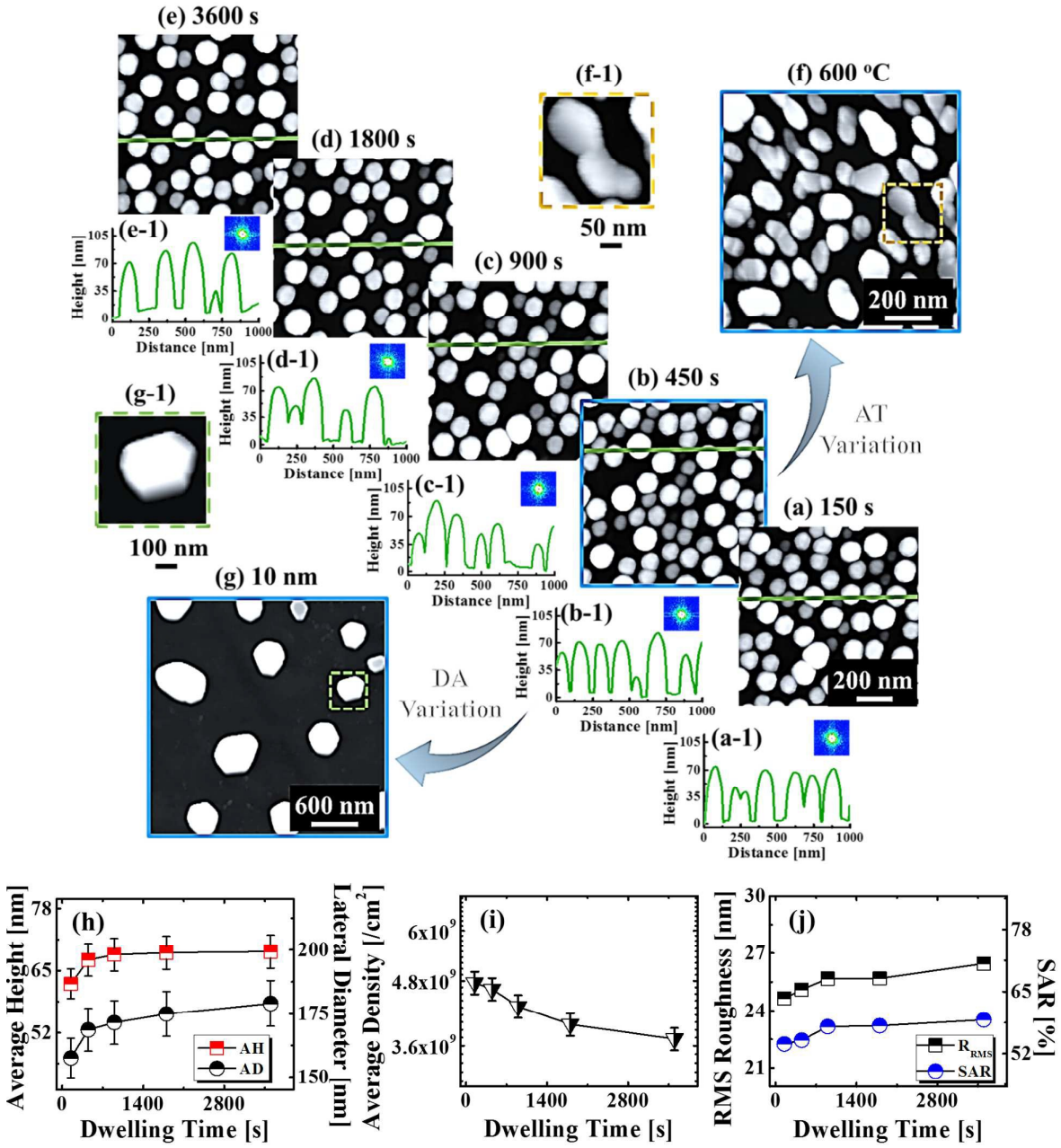


**Fig. 9** Self-assembled Au droplets with the control of dwelling times between 150 and 3600 s with 8 nm Au deposition at 800 °C on 4H-SiC (0001). (a) - (e) AFM top-views of 1 × 1 μm$^2$. (a-1) - (e-1) Cross-sectional line-profiles and 2-D FFT power spectra. (f) and (f-1) Au nano-mounds fabricated at 600 ˚C with the constant deposition amount and dwelling time of 8 nm and 450 s. (g) and (g-1) Au nano-crystals fabricated with the 10 nm Au deposition at fixed annealing temperature and dwelling time of 800 °C for 450 s. (f) 1 × 1 μm$^2$. (f-1) 250 × 250 nm$^2$. (g) 3 × 3 μm$^2$ and (g-1) 500 × 500 nm$^2$. (h) and (i) Plots of the AH, LD and AD with the error bars of ± 5%. (j) Plot of the $R_{RMS}$ and SAR.

**TOC image**

Hexagonal Au nano-crystals, round dome shaped droplets and irregular nano-mounds were fabricated on GaN (001) based on the combinational effects of thermal dewetting and surface free energy minimization with the systematic control of growth parameters.